# Closed-loop Control of the Safety Factor Profile in the TCV Tokamak

Justin E. Barton, Eugenio Schuster, Federico Felici and Olivier Sauter

***Abstract*— A key property that has a close relationship to both the performance and stability of the plasma in nuclear fusion tokamak devices is the safety factor profile ($q$-profile). As a result, extensive research has been conducted to develop algorithms to actively control the $q$-profile evolution with the goal of optimizing the tokamak approach to fusion energy production. The actuators that can be used to control the $q$-profile are the total plasma current, the auxiliary heating/current-drive system and the line-average electron density. In this work, we first investigate the effect that pure plasma auxiliary heating has on the $q$-profile in low performance (L-mode) operating scenarios in the TCV tokamak. This study indicates that pure auxiliary heating has a small effect on the $q$-profile in the examined scenarios. Therefore, feedback controllers that utilize the total plasma current and exclusively the auxiliary current-drive capabilities are designed for $q$-profile control in TCV. The controllers are designed to put emphasis on achieving the target $q$-profile in different spatial regions and to respond differently to errors in the $q$-profile. The control performance of each controller is tested with the simplified physics-based plasma profile simulation code RAPTOR. The comparison of the closed-loop performance of these controllers is done in preparation for future $q$-profile control experiments in the TCV tokamak.**

## I. Introduction

In order for two nuclei to fuse, they must be heated to extremely high temperatures so that they possess enough kinetic energy to overcome the Coulombic repulsion force that exists between them. At these temperatures, the fusion fuel (deuterium and tritium) is in the plasma state and therefore can conduct electrical current and interact with magnetic fields. The tokamak [1] concept for nuclear fusion energy production exploits this property of the plasma and uses externally applied magnetic fields to confine the plasma and create the conditions necessary for fusion to occur.

The ITER project is the next phase in the development of tokamak technology. There are many challenging control problems related to both stabilization/suppression of plasma instabilities and performance optimization of the plasma that need to be addressed in order for ITER to meet its demanding performance objectives (see [2], [3] for an introduction to many of these control problems). The safety factor profile ($q$-profile) [1] is a key plasma property related to both the plasma performance [4], [5] and stability [6], [7]. As a result, extensive research has been conducted to develop algorithms to actively control the $q$-profile evolution. Advances towards developing first-principles-driven (FPD), physics-model-based algorithms for $q$-profile control are discussed in [8]–[21]. Experiments in low confinement (L-mode) [1] scenarios in the DIII-D tokamak represent the first successful demonstration of FPD, physics-model-based closed-loop control of the entire $q$-profile [12], [14], [18]. The philosophy employed at DIII-D has recently been extended to control the $q$-profile in reactor relevant high confinement (H-mode) [1] scenarios in the ITER and DIII-D tokamaks [17], [19]–[21].

The total plasma current, the auxiliary heating/current-drive (H&CD) system and the line-average electron density are the actuators that can be utilized for $q$-profile control. In this work, we first investigate the effect that pure plasma auxiliary heating has on the $q$-profile in L-mode operating scenarios in the TCV tokamak by utilizing the RAPTOR code [22], which is a simplified physics-based code that simulates the $q$-profile and electron temperature profile evolution. This study indicates that pure auxiliary heating has a small effect on the $q$-profile in the examined scenarios. Therefore, we design feedback controllers that utilize the total plasma current and exclusively the current-drive capabilities of the auxiliary sources to control the $q$-profile in TCV. The controllers are designed to put emphasis on achieving the target $q$-profile in different spatial regions as well as to respond differently to errors in the $q$-profile. The closed-loop control performance of each controller is tested through simulations with the RAPTOR code. The comparison of the performance of these controllers is done in preparation for future $q$-profile control experiments in TCV.

## II. Plasma Heating Effect on the Safety Factor Profile

The evolution of the poloidal magnetic flux in a tokamak plasma is given by the magnetic diffusion equation [23]

$$\frac{\partial \psi}{\partial t} = \frac{\eta(T_e)}{\mu_0 \rho_b^2 \hat{F}^2} \frac{1}{\hat{\rho}} \frac{\partial}{\partial \hat{\rho}} \left( \hat{\rho} \hat{F} \hat{G} \hat{H} \frac{\partial \psi}{\partial \hat{\rho}} \right) + R_0 \hat{H} \eta(T_e) j_{ni}, \quad (1)$$

with boundary conditions $\frac{\partial \psi}{\partial \hat{\rho}}(0,t) = 0$, $\frac{\partial \psi}{\partial \hat{\rho}}(1,t) = -k_{I_p} I_p(t)$, where $\psi$ is the poloidal stream function, which is closely related to the poloidal magnetic flux $\Psi$ ($\Psi = 2\pi\psi$), $t$ is the time, $\eta$ is the plasma resistivity, $T_e$ is the electron temperature, $\mu_0$ is the vacuum magnetic permeability, $j_{ni}$ is the total noninductive current density, $k_{I_p}$ is a geometric constant and $I_p$ is the total plasma current. The spatial coordinate $\hat{\rho} = \rho/\rho_b$ is used to index the magnetic flux surfaces in the plasma, where $\rho$ is the mean effective minor radius of a magnetic flux surface, i.e., $\Phi(\hat{\rho}) = \pi B_{\phi,0} \rho^2$, $\Phi$ is the toroidal

This work was supported by the U.S. Department of Energy (DE-SC0001334 and DE-SC0010661). J.E. Barton (justin.barton@lehigh.edu) and E. Schuster (schuster@lehigh.edu) are with the Department of Mechanical Engineering and Mechanics, Lehigh University, Bethlehem, PA 18015, USA. F. Felici is with the Control Systems Technology Group, Eindhoven University of Technology, 5600 MB Eindhoven, The Netherlands. O. Sauter is with the École Polytechnique Fédérale de Lausanne (EPFL), Centre de Recherches en Physique des Plasmas (CRPP), Association EURATOM-Suisse, 1015 Lausanne, Switzerland.

magnetic flux, $B_{\phi,0}$ is the vacuum toroidal magnetic field at the geometric major radius $R_0$ of the tokamak and $\rho_b$ is the mean effective minor radius the last closed magnetic flux surface. The parameters $\hat{F}$, $\hat{G}$ and $\hat{H}$ are geometric spatial factors pertaining to the magnetic configuration of a particular plasma equilibrium. The $q$-profile is related to the poloidal magnetic flux as

$$q(\hat{\rho},t) = -d\Phi/d\Psi = -\left[B_{\phi,0}\rho_b^2\hat{\rho}\right]/\left[\partial\psi/\partial\hat{\rho}\right]. \quad (2)$$

In the development of the RAPTOR code [22], the magnetic diffusion equation (1) is combined with physics-based models of varying degrees of complexity for the electron density and temperature profiles, the plasma resistivity and the noninductive current sources to yield a model of the $q$-profile dynamics suitable for control design. To illustrate the effect that the electron temperature, and hence pure plasma heating, has on these plasma properties, we briefly describe the physics-based models. The plasma resistivity scales inversely with the electron temperature as

$$\eta(\hat{\rho},t) \propto T_e(\hat{\rho},t)^{-3/2}. \quad (3)$$

The total noninductive current is generated by the auxiliary sources and the bootstrap current (a self-generated noninductive source of plasma current) [24], i.e.,

$$j_{ni}(\hat{\rho},t) = j_{aux}^{tot}(\hat{\rho},t) + j_{bs}(\hat{\rho},t) = \sum_{i=1}^{n_{aux}} j_{aux,i}(\hat{\rho},t) + j_{bs}(\hat{\rho},t), \quad (4)$$

where $j_{aux}^{tot}$ is the total current density driven by the auxiliary sources, $j_{bs}$ is the current density driven by the bootstrap current, $j_{aux,i}$ is the current density driven by the individual auxiliary sources and $n_{aux}$ is the number of auxiliary sources. The individual auxiliary current-drives are modeled as

$$j_{aux,i}(\hat{\rho},t) = j_{aux,i}^{ref}(\hat{\rho})[T_e(\hat{\rho},t)/n_e(\hat{\rho},t)]P_{aux,i}(t), \quad (5)$$

where $j_{aux,i}^{ref}$ is a normalized reference deposition profile for the $i$-th auxiliary source, the term $T_e/n_e$ represents the current-drive efficiency, $n_e$ is the electron density and $P_{aux,i}$ is the $i$-th auxiliary power. The bootstrap current arises from the plasma radial pressure gradient that is produced by the magnetic confinement and is modeled as [25], [26]

$$j_{bs}(\hat{\rho},t) = \frac{k_{JkeV}R_0}{\hat{F}}\left(\frac{\partial\psi}{\partial\hat{\rho}}\right)^{-1}\left[2\mathscr{L}_{31}T_e\frac{\partial n_e}{\partial\hat{\rho}} + \{2\mathscr{L}_{31}+\mathscr{L}_{32}+\alpha\mathscr{L}_{34}\}n_e\frac{\partial T_e}{\partial\hat{\rho}}\right], \quad (6)$$

where $\mathscr{L}_{31}$, $\mathscr{L}_{32}$, $\mathscr{L}_{34}$ and $\alpha$ depend on the magnetic configuration of a particular plasma equilibrium, $k_{JkeV} = 1.602\times10^{-16}$ J/keV and we have assumed the electron and ion densities and temperatures, respectively, are equal.

The auxiliary H&CD actuators considered in this work are 4 electron cyclotron (gyrotron) launchers that are grouped into 2 clusters (denoted as $a$ and $b$). The deposition profiles for each source are shown in Fig. 1. The gyrotrons in cluster $a$ are: 1 on-axis co-current-injection ($j_{ec_{1a}}^{ref}$ in Fig. 1) and 1 off-axis counter-current-injection ($j_{ec_{2a}}^{ref}$ in Fig 1). The gyrotrons in cluster $b$ are: 1 on-axis counter-current-injection ($j_{ec_{1b}}^{ref}$ in Fig. 1) and 1 off-axis co-current-injection ($j_{ec_{2b}}^{ref}$ in

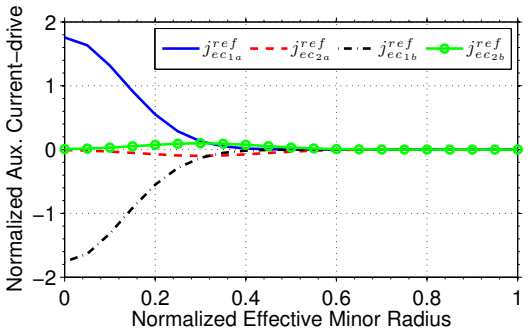


Fig. 1. Normalized auxiliary current-drive $\left(10^{20}\ \frac{\mathrm{m}^{-3}}{\mathrm{keV\cdot W}}\cdot\frac{\mathrm{A}}{\mathrm{m}^2}\right)$ in TCV.

Fig. 1). As a result, there are two limiting auxiliary H&CD conditions that can be achieved with this configuration. The first condition is related to plasma heating power ($P_{aux}^h$) and is associated with the sum of the powers injected through the gyrotron clusters, i.e., $P_{aux}^h = 2(P_{ec_a} + P_{ec_b})$. The second condition is related to plasma current-drive power ($P_{aux}^{cd}$) and is associated with the difference of the powers injected through the gyrotron clusters, i.e., $P_{aux}^{cd} = P_{ec_a} - P_{ec_b}$. Note that if $P_{ec_a} = P_{ec_b}$, the auxiliary current-drive would be zero as $j_{ec_{1b}}^{ref} = -j_{ec_{1a}}^{ref}$ and $j_{ec_{2b}}^{ref} = -j_{ec_{2a}}^{ref}$, i.e., pure plasma heating.

### A. Auxiliary Heating in Presence of Auxiliary Current-drive

We investigate the effect that auxiliary heating has on the $q$-profile in the presence of constant auxiliary current-drive using RAPTOR by allowing the plasma to evolve to a stationary state with a constant current-drive power $P_{aux}^{cd} = -0.1$ MW under moderate heating conditions ($P_{aux}^h =$ 1.0 MW) and high heating conditions ($P_{aux}^h = 1.6$ MW) at two values of plasma current, $I_p = 140$ kA and $I_p = 185$ kA, respectively. The power injected through either of the clusters in TCV is constrained to the range 0.2 MW $\leq P_{ec_i} \leq$ 0.45 MW, for $i \in$ [a,b]. A comparison of the auxiliary and bootstrap current densities before and after the heating power is increased is shown in Figs. 2(a-b). At both values of total plasma current, increasing the electron temperature through heating increases (in magnitude) both the auxiliary (Fig. 2(a)) and bootstrap (Fig. 2(b)) current-drives as expected from (5)-(6). The effect that the increases in both on-axis auxiliary counter-current-drive (in negative direction) and off-axis bootstrap co-current-drive (in positive direction), and the decrease in the plasma resistivity (from (3)) has on the $q$-profile is shown in Fig. 2(c). From Fig. 2(c), we see that auxiliary heating in the presence of constant auxiliary current-drive results in approximately a 5% increase in the $q$-profile in the region $\hat{\rho} \in [0, 0.2]$ with a negligible change outside this spatial region. This is also the region where the auxiliary current-drive has increased in magnitude (Fig. 2(a)).

### B. Auxiliary Heating in Absence of Auxiliary Current-drive

To study the relative importance of the current-drive mechanisms (auxiliary and bootstrap), we investigate the effect that auxiliary heating has on the $q$-profile in the absence of auxiliary current-drive using RAPTOR by allowing the plasma to evolve to a stationary state with no current-drive power $P_{aux}^{cd} = 0$ MW under low heating conditions ($P_{aux}^h =$

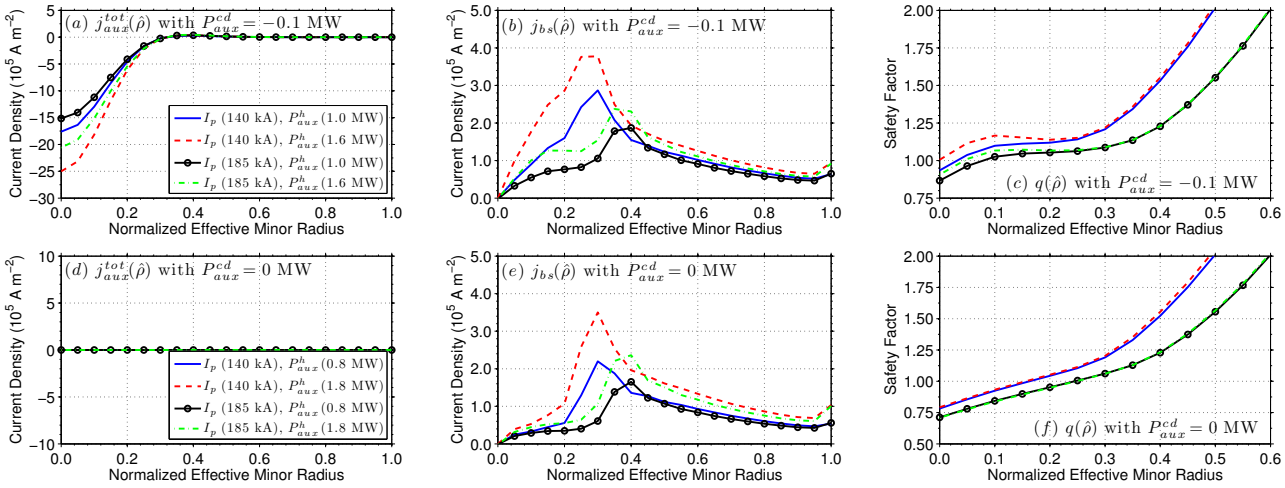


Fig. 2. Comparison of stationary state plasma parameters under low and high plasma heating conditions with (a-c) $P_{aux}^{cd} = -0.1$ MW and (d-f) $P_{aux}^{cd} = 0$ MW.

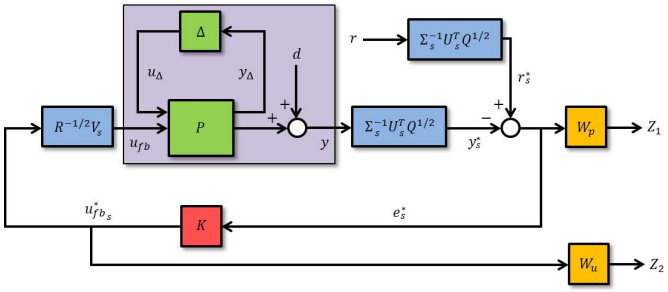


Fig. 3. Schematic of $q$-profile feedback control problem formulation.

0.8 MW) and high heating conditions ($P_{aux}^h = 1.8$ MW) at two values of plasma current, $I_p = 140$ kA and $I_p = 185$ kA, respectively. A comparison of the auxiliary and bootstrap current densities before and after the heating power is increased is shown in Figs. 2(d-e). Since $P_{aux}^{cd} = 0$ MW, there is no auxiliary current-drive (Fig. 2(d)). Again, at both values of total plasma current, increasing the electron temperature through heating increases the bootstrap current (Fig. 2(e)) as expected from (6). By comparing Fig. 2(b) and Fig. 2(e), we see that the bootstrap current-drive behaves in a similar fashion in response to auxiliary heating independent of the presence or absence of auxiliary current-drive. However, the increase in off-axis bootstrap co-current-drive and the decrease in plasma resistivity (from (3)) results in a small change in the $q$-profile as shown in Fig. 2(f) when auxiliary heating is applied without auxiliary current-drive.

## III. Feedback Control Design

As shown in the previous section, auxiliary heating has a small effect on the $q$-profile in the absence of auxiliary current-drive in the considered TCV scenarios. As a result, a $q$-profile feedback controller that utilizes the total plasma current and exclusively the current-drive capabilities of the auxiliary sources is designed by employing the method in [17], [19], and the controller will attempt to counteract any $q$-profile disturbance that results from plasma heating effects.

### A. Partial Differential Equation Model

We begin by defining ranges in which the electron density profile, the electron temperature profile and the plasma resistivity are expected to be in typical TCV L-mode scenarios. These parameters are modeled as

$$n_e(\hat{\rho},t) = n_e^{nom}(\hat{\rho}), \tag{7}$$

$$T_e(\hat{\rho},t) = T_e^{nom}(\hat{\rho}) + T_e^{unc}(\hat{\rho})\delta_{T_e}(t), \tag{8}$$

$$\eta(\hat{\rho},t) = \eta^{nom}(\hat{\rho}) + \eta^{unc}(\hat{\rho})\delta_{T_e}(t), \tag{9}$$

where $(\cdot)^{nom}$ represents a nominal profile, $(\cdot)^{unc}$ represents an uncertain profile and $|\delta_{T_e}| \leq 1$. Note that the dependence of the plasma resistivity on the electron temperature is modeled to first order to simplify the control design. Also, note that an uncertainty in the electron density profile can readily be incorporated in the formulation of the model [17], [19], but for the scenarios considered, the electron density profile is assumed constant. By combining the magnetic diffusion equation (1) with the noninductive current-drive models (4)-(6) and the uncertain models (7)-(9), we obtain

$$\begin{aligned}\frac{\partial \psi}{\partial t} = {} & \frac{(\eta^{nom} + \eta^{unc}\delta_{T_e})}{\mu_0 \rho_b^2 \hat{F}^2} \frac{1}{\hat{\rho}} \frac{\partial}{\partial \hat{\rho}} \left( \hat{\rho} \hat{F} \hat{G} \hat{H} \frac{\partial \psi}{\partial \hat{\rho}} \right) \\ & + \frac{R_0 \hat{H} (\eta^{nom} + \eta^{unc}\delta_{T_e})(T_e^{nom} + T_e^{unc}\delta_{T_e})}{n_e^{nom}} \\ & \times \left\{ \left( j_{ec_{1a}}^{ref} + j_{ec_{2a}}^{ref} \right) P_{ec_a}(t) + \left( j_{ec_{1b}}^{ref} + j_{ec_{2b}}^{ref} \right) P_{ec_b}(t) \right\} \\ & + \frac{k_{JeV} R_0^2 \hat{H} (\eta^{nom} + \eta^{unc}\delta_{T_e})}{\hat{F}} \left( \frac{\partial \psi}{\partial \hat{\rho}} \right)^{-1} \\ & \times \left[ 2\mathscr{L}_{31} (T_e^{nom} + T_e^{unc}\delta_{T_e}) \frac{\partial}{\partial \hat{\rho}} \{ n_e^{nom} \} \right. \\ & \left. + \{ 2\mathscr{L}_{31} + \mathscr{L}_{32} + \alpha \mathscr{L}_{34} \} n_e^{nom} \frac{\partial}{\partial \hat{\rho}} \{ T_e^{nom} + T_e^{unc}\delta_{T_e} \} \right]. \end{aligned} \tag{10}$$

### B. Model Reduction via Spatial Discretization

From (2), we see that the rotational transform profile ($\iota = 1/q$) is dependent on the poloidal flux gradient profile, which we define as $\theta(\hat{\rho},t) \equiv [\partial\psi/\partial\hat{\rho}(\hat{\rho},t)]$. After some mathematical manipulations, a PDE model of the $\theta$ profile dynamics can be obtained from (10). Spatially discretizing this model by employing a finite difference method results in an ordinary differential equation model defined by

$$\dot{x} = f_\theta(x,u,\delta) \qquad y_i = -\frac{1}{B_{\phi,0}\rho_b^2 \hat{\rho}_i} x_i, \tag{11}$$

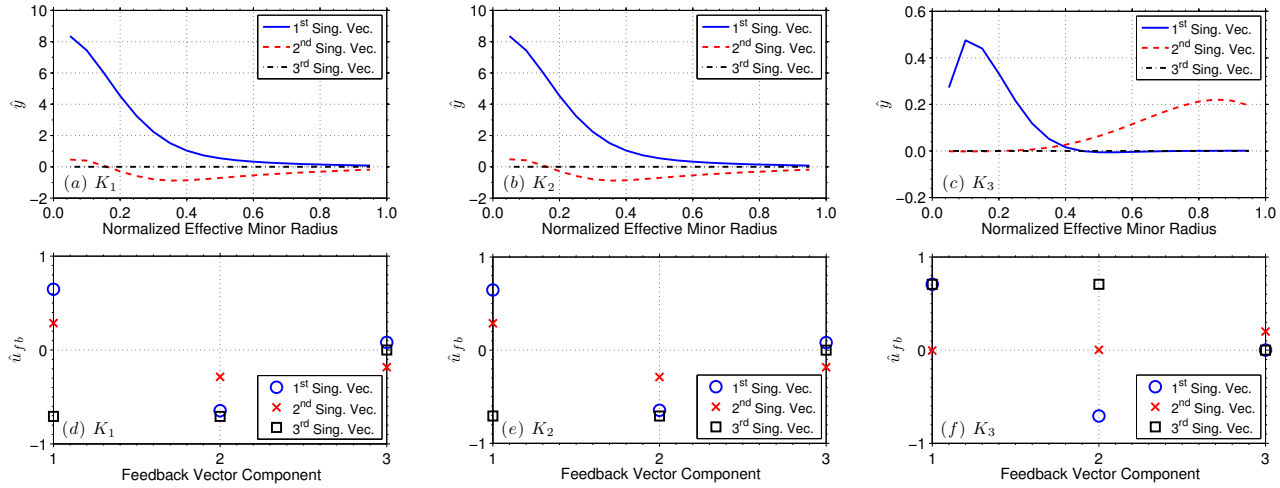


Fig. 4. Relevant control channels: (a-c) output ($\hat{y} = Q^{-1/2}U\Sigma\hat{y}^*$) and (d-f) input ($\hat{u}_{fb} = R^{-1/2}V\hat{u}^*_{fb}$). Note $u_{fb} = \left[P_{ec_a}, P_{ec_b}, I_p\right]|_{fb}$.

where $x = [\theta_i] \in \mathbb{R}^{n_\theta}$ is the state vector, $y = [\iota_i] \in \mathbb{R}^{n_\theta}$ is the output vector, $\theta_i$, $\iota_i$ and $\hat{\rho}_i$ are the values of $\theta$, $\iota$ and $\hat{\rho}$ at the discrete nodes, for $i = [2, \ldots, m_\theta - 1]$, $u = [P_{ec_a}, P_{ec_b}, I_p] \in \mathbb{R}^3$ is the control input vector, $\delta = \left[\delta_{T_e}, \delta^2_{T_e}\right] \in \mathbb{R}^2$ is the uncertain parameter vector, $f_\theta \in \mathbb{R}^{n_\theta}$ is a nonlinear function, $n_\theta = m_\theta - 2$, and $m_\theta$ is the number of nodes utilized to represent the spatial domain. After linearizing (11) with respect to the state and control input around a nominal operating point $(x_{eq}, u_{eq})$ characterized by $\delta = 0$, i.e., $f(x_{eq}, u_{eq}, 0) = 0$, we obtain

$$\dot{\tilde{x}} = A(\delta)\tilde{x} + B(\delta)u_{fb} + d_\delta \qquad y = C\tilde{x} + Du_{fb}, \tag{12}$$

where $\tilde{x} = x - x_{eq}$, $u_{fb} = u - u_{eq}$, $d_\delta = f(x_{eq}, u_{eq}, \delta)$, $A(\delta)$ and $B(\delta)$ are the Jacobians $\partial f_\theta / \partial x \in \mathbb{R}^{n_\theta \times n_\theta}$ and $\partial f_\theta / \partial u \in \mathbb{R}^{n_\theta \times 3}$ evaluated at $(x_{eq}, u_{eq})$, $C = \text{diag}\{-1/(B_{\phi,0}\rho_b^2\hat{\rho}_i)\} \in \mathbb{R}^{n_\theta \times n_\theta}$ and $D = 0$.

### C. Identification of Relevant Control Channels

As there are only three control inputs, we can at most independently control three linear combinations of the system output. Therefore, we obtain the most relevant control channels from the nominal input-output relation at a particular frequency $j\omega_{dc}$, which is expressed as $\hat{y} = \hat{G}_0\hat{u}_{fb} = Q^{-1/2}\tilde{G}_0R^{1/2}\hat{u}_{fb} = Q^{-1/2}U\Sigma V^T R^{1/2}\hat{u}_{fb}$. The decoupled output and input are denoted by $\hat{y}^* = \Sigma^{-1}U^TQ^{1/2}\hat{y}$ and $\hat{u}^*_{fb} = V^TR^{1/2}\hat{u}_{fb}$, i.e., $\hat{y}^* = \hat{u}^*_{fb}$. The nominal system transfer function is expressed as $G_0(s) = C\left(sI_{n_\theta} - A(0)\right)^{-1}B(0)$ and $\hat{G}_0$ denotes the real approximation of the complex matrix $G_0(j\omega_{dc})$ [27]. The positive definite matrices $Q \in \mathbb{R}^{n_\theta \times n_\theta}$ and $R \in \mathbb{R}^{3\times 3}$ are utilized to weight the relative tracking performance and control effort. Finally, the "weighted" transfer function $\tilde{G}_0$ and its economy size singular value decomposition are defined as $\tilde{G}_0 = Q^{1/2}\hat{G}_0R^{-1/2} = U\Sigma V^T$, where $\Sigma \in \mathbb{R}^{3\times 3}$ is a diagonal matrix of singular values and $U \in \mathbb{R}^{n_\theta \times 3}$ and $V \in \mathbb{R}^{3\times 3}$ are matrices that possess the following properties $V^TV = VV^T = I, U^TU = I$. Some of the singular values may have a small magnitude relative to the others and may be chosen to be neglected in the control synthesis. Quantities associated with the significant singular values are denoted by a subscript $s$ for the remainder of this paper, i.e., $(\cdot)_s$.

### D. Feedback Control Problem Formulation

The feedback control problem is formulated as shown in Fig. 3, where $r$ is the reference value, the tracking error is defined as $e = r - y$ and $K$ is the to-be-designed feedback controller. The feedback system (12) is written in the conventional $P - \Delta$ robust control framework, where $P$ is the generalized transfer function and $\Delta = \text{diag}\{\delta_{T_e}\}$ is a structured uncertainty matrix, by employing the method described in [28]. The closed-loop system outputs are $Z_1$ and $Z_2$ and the frequency dependent weight functions $W_p$ and $W_u$ are utilized to optimize the feedback performance. The control problem is formulated as (see Fig. 3)

$$\min_K \left|\left|T_{zw}\right|\right|_\infty, \ \forall\omega \qquad T_{zw} = \begin{bmatrix} W_pS_{DC_O} & -W_pS_{DC_O} \\ W_uKS_{DC_O} & -W_uKS_{DC_O} \end{bmatrix}, \tag{13}$$

where $T_{zw}$ is the closed-loop transfer function from the inputs $(r^*_s, d^*_s)$ to the outputs $(Z_1, Z_2)$, $d^*_s = \Sigma_s^{-1}U_s^TQ^{1/2}d$, $S_{DC_O} = (I + \Sigma_s^{-1}U_s^TQ^{1/2}P_{22}R^{-1/2}V_sK)^{-1}$ and $P_{22}$ is the component transfer function of $P$ from $u_{fb}$ to $y$. The feedback controller $K$ is obtained by solving (13) and is designed such that the closed-loop system is stable for all allowable perturbations (checked by computing the structured singular value [27]).

## IV. Comparison of Control Algorithm Performance in TCV RAPTOR Simulations

In this section, the closed-loop performances of three feedback controllers are compared in TCV L-mode scenarios using RAPTOR [22]. The relevant control channels of the first controller (denoted as $K_1$) are evaluated at a frequency of $\omega_{dc} = 0$ rad/s with emphasis placed on achieving the target $q$-profile in $\hat{\rho} \in [0, 0.4]$. The second controller (denoted as $K_2$) is designed in the same way as controller $K_1$ but with emphasis placed on achieving the target $q$-profile in $\hat{\rho} \in [0, 0.4]$ and $\hat{\rho} \in [0.7, 0.8]$. Finally, the relevant control channels of the third controller (denoted as $K_3$) are evaluated at a frequency of $\omega_{dc} = 1500$ rad/s with emphasis placed on achieving the target $q$-profile in $\hat{\rho} \in [0, 0.4]$ and $\hat{\rho} \in [0.7, 0.8]$. The relevant control channels of the three controllers are shown in Fig. 4. First, we note that the third actuation direction (□) for all of the controllers (Figs. 4(d-f)) is associated

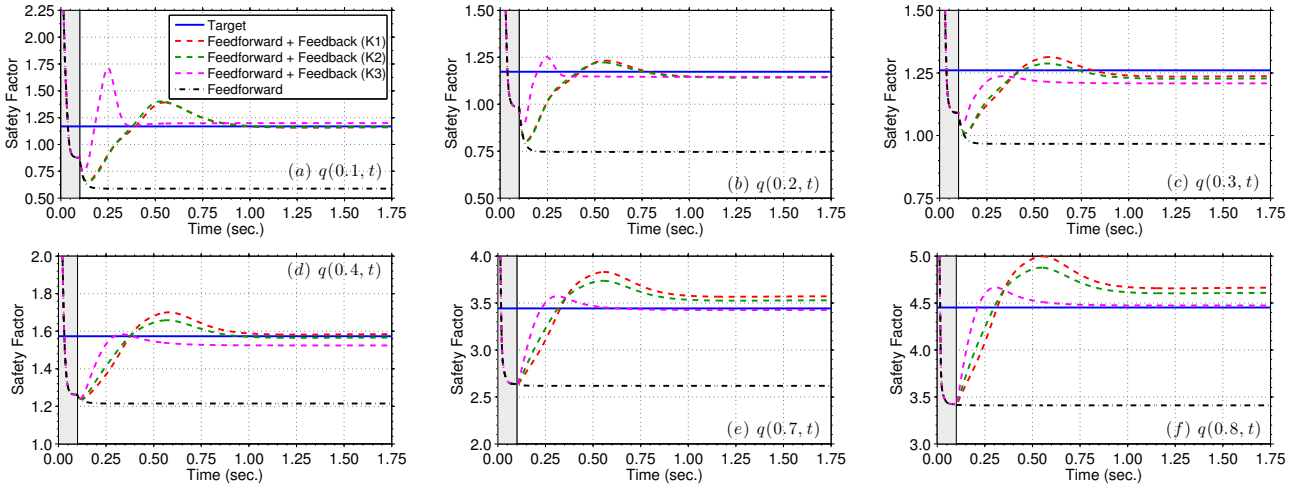


Fig. 5. Time traces of $q$ at various radial locations. Gray-shaded region denotes when feedback controller is off.

with auxiliary heating (equal contributions from $P_{ec_a}$ and $P_{ec_b}$ in the same direction and no contribution from $I_p$), which is negligible in this control design approach. Second, we see that the control inputs are coupled for controllers $K_1$ and $K_2$, i.e., the first ($\circ$) and second ($\times$) input singular vectors have contributions from all three actuators (Figs. 4(d-e)). In contrast, the gyrotron and total plasma current actuation directions are decoupled for controller $K_3$ (Fig. 4(f)), i.e., the first singular vector only has contributions from $P_{ec_a}$ and $P_{ec_b}$ and the second singular vector only has a contribution from $I_p$. The bandwidth of the gyrotron control direction for controller $K_3$ is set at a slightly higher value relative to the other control directions. This is enabled because the actuation directions are decoupled in controller $K_3$.

### A. One Target Simulation

A $q$-profile achieved in TCV with a total plasma current of 140 kA and counter-current-injection auxiliary power is chosen as the target. First, a nominal $q$-profile evolution is obtained by executing a feedforward-only simulation with a nominal set of input trajectories. Next, the ability of each of the controllers to track the target is determined by executing feedforward + feedback simulations with the nominal inputs.

Time traces of $q$ at various spatial locations are shown in Fig. 5. Once the controllers become active, they are able to drive the $q$-profile towards the target. The controller $K_3$ is able to respond to the error in the plasma core faster than controllers $K_1$ and $K_2$ due to the slightly higher bandwidth of the gyrotron control direction for controller $K_3$. Additionally, the error near the plasma boundary is eliminated by controller $K_3$, whereas there is a small tracking error obtained with controllers $K_1$ and $K_2$. However, the error near the plasma boundary obtained with controller $K_2$ is smaller than the error obtained with controller $K_1$ due to the higher weight placed on achieving the target in this spatial region for controller $K_2$.

### B. Two Target Simulation

A $q$-profile achieved in TCV with a total plasma current of 140 kA and co-current-injection auxiliary power is chosen as the target during the time interval $t \in [0, 0.9]$ s. During the time interval $t \in [1.0, 1.75]$ s, a $q$-profile achieved in TCV with a total plasma current of 190 kA and counter-current-injection auxiliary power is chosen as the target. The target during the time interval $t \in (0.9, 1.0)$ s is obtained by linear interpolation. First, a nominal $q$-profile evolution is obtained by executing a feedforward-only simulation with a nominal set of input trajectories. Next, the ability of each of the controllers to track the target is determined by executing feedforward + feedback simulations with the nominal inputs.

Time traces of $q$ at various spatial locations and a comparison of the inputs are shown in Fig. 6. Once the controllers become active, they drive the $q$-profile towards the first target. In tokamaks, the local $q$-value is roughly inversely related to the local current density amplitude. In the feedback-controlled simulations, all of the controllers decrease the total plasma current and the cluster-$a$ gyrotron power, while increasing the cluster-$b$ gyrotron power to track the first target. For controllers $K_1$ and $K_2$ the actuators are utilized to control the $q$-profile across the entire spatial domain (Figs. 4(a-b)). Therefore, in response to the $q$-value being above the target at $\hat{\rho} = 0.2, 0.3$ (current density to low), the controllers $K_1$ and $K_2$ increase the total plasma current (relative to controller $K_3$) to lower the $q$-value at these locations (the current density at these locations will increase as the current applied at the plasma boundary propagates towards the plasma core). As a result of the increased current density, a tracking error at $\hat{\rho} = 0.4, 0.7, 0.8$ is obtained with controllers $K_1$ and $K_2$. However, the error obtained with controller $K_2$ is smaller than the error obtained with controller $K_1$ (see section IV-A). In contrast, for controller $K_3$, the gyrotrons are utilized to control the $q$-profile in the plasma core and the total plasma current is utilized to control the $q$-profile near the plasma boundary (Fig. 4(c)). Therefore, controller $K_3$ does not increase the total plasma current to decrease the error at $\hat{\rho} = 0.2, 0.3$, and as a result, good tracking performance is achieved at $\hat{\rho} = 0.4, 0.7, 0.8$. When the target profile is switched, a similar tracking performance is achieved in the plasma core ($\hat{\rho} = 0.1, 0.2, 0.3$) with all of the controllers. Finally, with controllers $K_1$ and $K_2$ a smaller error at $\hat{\rho} = 0.4$ is obtained at the expense of achieving a larger error at $\hat{\rho} = 0.7, 0.8$ (relative to controller $K_3$).

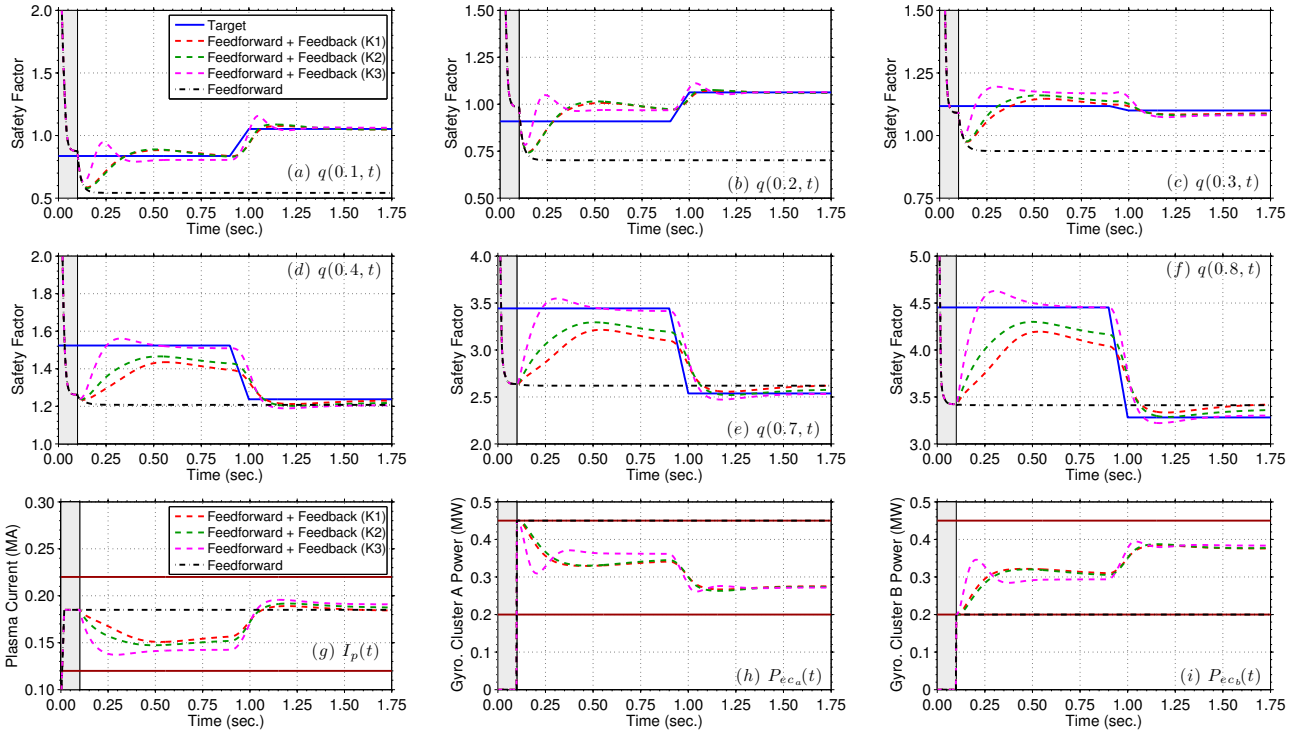


Fig. 6. Time traces of outputs ($q$) and inputs ($I_p, P_{ec_a}, P_{ec_b}$). Gray-shaded region denotes when feedback controller is off. Actuator limits (solid brown).

## V. Conclusions and Future Work

Auxiliary heating was shown to have a relatively small effect on the $q$-profile in the absence of auxiliary current-drive in the studied TCV scenarios. As a result, we designed feedback controllers that exclusively utilized the current-drive capabilities of the auxiliary sources to control the $q$-profile in TCV. The algorithms were designed to put emphasis on achieving the target $q$-profile in different spatial regions and to respond differently to errors in the $q$-profile. The closed-loop performance of each controller was tested and compared through simulations with the RAPTOR code. Our future work includes testing the controllers experimentally in TCV by utilizing the closed-loop plasma state observer developed in [29] to reconstruct the $q$-profile in real-time.

## References


[1] WESSON, J., *Tokamaks*, Oxford, UK: Clarendon Press, 2004.
[2] PIRONTI, A. et al., IEEE Control Syst. Mag. **25** (2005) 30.
[3] WALKER, M. et al., IEEE Control Syst. Mag. **26** (2006) 35.
[4] WALTZ, R. E. et al., Physics of Plasmas **2** (1995) 2408.
[5] PETTY, C. C. et al., Physics of Plasmas **5** (1998) 1695.
[6] FERRON, J. et al., Physics of Plasmas **12** (2005) 056126.
[7] HENDER, T. C. et al., Nuclear Fusion **47** (2007) S128.
[8] OU, Y., XU, C., and SCHUSTER, E., IEEE Transactions on Plasma Science **38** (2010) 375.
[9] OU, Y., XU, C., and SCHUSTER, E., IEEE Trans. Control Syst. Technol. **19** (2011) 432.
[10] XU, C., OU, Y., and SCHUSTER, E., Automatica **47** (2011) 418.
[11] GAYE, O. et al., Sliding Mode Stabilization of the Current Profile in Tokamak Plasmas, in *50th IEEE Conference on Decision and Control*, pp. 2638–2643, 2011.
[12] BARTON, J. E., BOYER, M. D., SHI, W., SCHUSTER, E., et al., Nucl. Fusion **52** (2012) 123018.
[13] GAHLAWAT, A. et al., Bootstrap Current Optimization in Tokamaks using Sum-of-Squares Polynomials, in *51st IEEE Conference on Decision and Control*, pp. 4359–4365, 2012.
[14] BOYER, M. D., BARTON, J. E., SCHUSTER, E., et al., Plasma Phys. Control. Fusion **55** (2013) 105007.
[15] ARGOMEDO, F. et al., Nuclear Fusion **53** (2013) 033005.
[16] VU, N. M. T. et al., An IDA-PBC Approach for the Control of 1D Plasma Profile in Tokamaks, in *52nd IEEE Conference on Decision and Control*, pp. 4176–81, 2013.
[17] BARTON, J. E., BESSEGHIR, K., LISTER, J., and SCHUSTER, E., Robust Control of the Safety Factor Profile and Stored Energy Evolutions in High Performance Burning Plasma Scenarios in the ITER Tokamak, in *52nd IEEE Conference on Decision and Control*, pp. 4194–99, 2013.
[18] BOYER, M. D., BARTON, J. E., SCHUSTER, E., et al., IEEE Trans. Control Syst. Technol. **22** (2014) 1725.
[19] BARTON, J. E., BOYER, M. D., SHI, W., WEHNER, W. P., SCHUSTER, E., et al., Experimental and Simulation Testing of Physics-model-based Safety Factor Profile and Internal Energy Feedback Controllers in DIII-D Advanced Tokamak Scenarios, in *19th IFAC World Congress*, pp. 5223–5228, 2014.
[20] BOYER, M. D., BARTON, J. E., SHI, W., WEHNER, W. P., SCHUSTER, E., et al., Simultaneous Boundary and Distributed Feedback Control of the Current Profile in H-mode Discharges on DIII-D, in *19th IFAC World Congress*, pp. 1568–1573, 2014.
[21] WEHNER, W., SHI, W., BARTON, J., SCHUSTER, E., et al., First-Principles-Driven Model-Based Control of the Poloidal Magnetic Flux Profile at the DIII-D Tokamak, in *19th IFAC World Congress*, pp. 10319–10324, 2014.
[22] FELICI, F. et al., Nuclear Fusion **51** (2011) 083052.
[23] HINTON, F. and HAZELTINE, R., Rev. Mod. Phys. **48** (1976) 239.
[24] PEETERS, A. G., Plasma Phys. and Control. Fusion **42** (2000) B231.
[25] SAUTER, O. et al., Physics of Plasmas **6** (1999) 2834.
[26] SAUTER, O. et al., Physics of Plasmas **9** (2002) 5140.
[27] SKOGESTAD, S. and POSTLETHWAITE, I., *Multivariable Feedback Control Analysis and Design*, Wiley, New York, 2005.
[28] PACKARD, A., *Whats New with $\mu$: Structured Uncertainty in Multivariable Control*, PhD thesis, Univ. of Calif., Berkeley, 1988.
[29] FELICI, F. et al., A Dynamic State Observer for Real-time Reconstruction of the Tokamak Plasma Profile State and Disturbances, in *2014 American Control Conference*, pp. 4816–4823, 2014.